Supporting Information

Serres et al. 10.1073/pnas.1117412109

SI Text 1

It should be noted that the spatial resolution achievable in mice is considerably higher than the spatial resolution possible clinically and that, as voxel sizes increase, the number of microparticles of iron oxide (MPIO) per voxel must be higher to induce a detectable change in contrast. In the current study, the signal was entirely abolished in many of the voxels defined as having vascular cell adhesion molecule (VCAM)–MPIO-induced contrast effects (i.e., ~100% signal reduction), whereas the work of Shapiro et al. (1) indicated that only a 20% reduction in signal within a voxel is required for a detectable contrast effect. Clinical T2* data are now routinely acquired at ~1-mm isotropic resolution (or equivalent) at 3 T. If we assume that the distribution of MPIO per unit tumor area remains roughly constant as it grows, then based on detection of a 100-μm diameter tumor at 90-μm isotropic resolution, we would estimate that an ~650-μm diameter tumor could be detected at 1-mm resolution [100 × cube root (11.1 × 11.1 × 11.1 × 0.2) μm]. Moreover, we have shown that, as the tumor grows, VCAM-1 expression increases more rapidly than expected (Fig. 3 *A* and *B*), and as a result, the density of MPIO per unit tumor volume may, in fact, increase as the tumor grows.

Alternatively, the average number of contiguous voxels defined as hypointense at the current resolution (90 μm isotropic) that we could, therefore, consider to reflect a single metastasis was eight at day 10 (tumor diameter ~100 μm). Thus, the volume encompassed by the effects of VCAM–MPIO binding to a single metastasis was ~0.006 mm^3 (8 × 0.09 × 0.09 × 0.09 mm^3). If this volume was encompassed within a 1-mm^3 voxel, it would equate to an ~0.6% signal change. On this basis, we would require ~33 times the volume of VCAM–MPIO contrast effect to detect the signal change at 1-mm isotropic resolution, which would equate to an increase in tumor diameter of ~3.25 times (i.e., diameter = 300–350 μm).

Another factor that must be taken into consideration is whether the signal to noise (SNR) that is achievable at clinical field strengths in the time available (typically ~10-min acquisition) would be sufficient to enable detection of a 20% signal change. To reliably detect a 20% signal change, the SD within a pixel because of other fluctuations needs to be one-third of this 20% (i.e., 6.6%). This finding corresponds to an SNR of 15:1. To measure the attainable SNR, a 3D gradient echo (GE) dataset of the human brain with equivalent parameters to our mouse acquisitions modified for field strength (Fig. S4) and 1-mm isotropic resolution was acquired at 3 T in an acquisition time of 9.5 min (Fig. S4). The measured SNR was 21:1 for gray matter and 27:1 for white matter, which is more than sufficient SNR to allow detection of a 20% signal change owing to endovascular VCAM–MPIO retention.

Thus, although estimates only, these calculations suggest that, at clinical resolutions, brain metastases should be detectable considerably earlier than is currently possible. With the advent of higher field human scanners (7 T) and the more sensitive susceptibility-weighted imaging sequences (2), this detection sensitivity should improve, as recently shown by Grabner et al. (3); this work obtained susceptibility-weighted images of human brain at a resolution of 0.3 × 0.3 × 1.2 mm (3).

Interestingly, the move to lower clinical imaging resolutions has an important outcome with regards to the very low false-positive rate observed in naïve animals injected with VCAM–MPIO or day 10 4T1-injected animals given IgG–MPIO, which reflects either natural hypointensities in the brain or nonspecific MPIO retention. The average number of pixels encompassed by such nonspecific hypointensity is ~3.5, which would be undetectable at clinical imaging resolutions (calculations are shown above). Thus, the false-positive rate from nonspecific MPIO retention should effectively be zero if this approach is applied clinically, because there is no reason to believe that the volume associated with nonspecific MPIO should increase in man compared with mouse.

SI Text 2

Although we have found no histological evidence of inflammation or necrosis in any tissue (including liver, lung, heart, spleen, gut, and kidney) in response to VCAM–MPIO administration, to assess the possibility of systemic macrophage activation at the molecular level, we studied an additional set of animals. Female BALB/c mice (n = 3 per group) were injected i.v. with either VCAM–MPIO (4 mg Fe/kg body weight in 100 μL saline) or saline alone, and fresh liver was collected 4 h after injection to examine the acute phase response (APR) by quantitative PCR. Our previous work investigating the APR to acute brain injury has shown that this time is sufficient to generate a robust APR that includes up-regulation of TNF and classical acute phase proteins such as serum amyloid P (SAP) (4, 5), a major acute phase protein in all strains of mice. During acute chemical, physical, or inflammatory stimulus, the concentration of SAP can increase 50- to 100-fold within 24–48 h, and changes can be readily detected after 4 h. Measurement of the concentration of SAP is indicative of the extent and severity of an inflammatory stimulus and can be used to assess various modalities of treatment. RNA extraction and quantitative RT-PCR assays were performed on the liver samples as previously described from pieces of snap-frozen liver (6–8).

Interestingly, the level of expression of both TNF and SAP was reduced in the VCAM–MPIO-treated animals compared with controls (Fig. S5). This finding suggests that the phagocytosis of the circulating particles is associated with an antiinflammatory and not a proinflammatory phenotype. This outcome is certainly not true of all i.v.-administered particles; for example, administration of latex particles i.v., which results in phagocytosis by Kupffer cells and hepatic neutrophils, primes these cells to generate superoxide anion (9). However, others have shown ex vivo that feeding macrophages with particles of different types can induce an antiinflammatory phenotype (10), and our in vivo data seem to support this concept, indicating that macrophage activation is not a consequence of VCAM–MPIO administration.

MRI: Acquisition and Data Analysis. MRI data were acquired on a 7-T magnet with a Varian Inova spectrometer (Varian). For detection of VCAM–MPIO, a T_2*-weighted 3D GE dataset was acquired as follows: flip angle = 27°; repetition time (TR) = 65 ms; echo time (TE) = 7.5 ms; field of view = 11.2 × 22.5 × 22.5 mm; matrix size = 96 × 192 × 256; averages = 2; total acquisition time ~ 40 min. The midpoint of acquisition was 1.5 ± 0.2 h after MPIO injection. Data were zero-filled to 128 × 256 × 256 and reconstructed offline, giving a final isotropic resolution of 88 μm. Subsequently, a set of seven coronal T_1-weighted images (slice thickness = 1 mm) was acquired using a spin-echo sequence (TR = 500 ms; TE = 20 ms; field of view = 25 × 25 mm; matrix size = 128 × 128) both pre- and 5 min post-i.v. gadolinium-DTPA (Omniscan; GE Healthcare) injection (30 μL) was used to identify blood–brain barrier (BBB) permeability.

Each T_2*-weighted dataset was converted into .tiff images, manually masked to exclude extracerebral structures, and converted to 8-bit gray scale. Images were thresholded such that any pixels of signal intensity >3 SD below the mean intensity of normal brain were set to zero (black) and all others were set to one

(white). Signals arising from ventricles or sinuses, which appear hypointense naturally, were excluded by comparison with a naïve animal with no contrast agent. The masked and thresholded images were stacked into a single sequence in ImagePro (Media Cybernetic), and MPIO binding, defined as all pixels with signal levels of zero, was quantified. Segmented images were reconstructed to visualize the spatial distribution of MPIO binding, with low-signal areas assigned to the red channel. Voxel volumes were summed and expressed as raw volumes in microliters.

Immunohistochemistry and Immunofluorescence: Mouse Tissue. After MRI, animals were transcardially perfused under terminal anesthesia with 0.9% heparinized saline followed by 200 mL of either 4% paraformaldehyde or periodate lysine paraformaldehyde containing only 0.1% glutaraldehyde. The brains were postfixed, cryoprotected, embedded, and frozen in isopentane at −20°. Some of the brains were used for immunohistochemical analysis of tumor number and area ($n = 3$–4 per time point), whereas the others were used for assessment of VCAM-1 expression using either immunohistochemistry or immunofluorescence. All incubations were performed at room temperature, unless otherwise stated.

For immunohistochemical detection of tumors, 10-μm sections were quenched with 1% hydrogen peroxide in methanol (Sigma Aldrich) and blocked with 1% normal rabbit serum (Vector Laboratories) for 1 h. Sections were incubated with primary GFP antibody (1:1,000; Abcam) for 1 h, washed using PBS/0.01% Tween (Sigma Aldrich), and then incubated with a biotinylated rabbit polyclonal to chicken IgY secondary antibody (1:1,000; Abcam) for 1 h. Slides were washed and then incubated in Vectorelite ABC kit (1:1:100; Vector Laboratories) for 45 min. The peroxidase was visualized using 3,3′-diaminobenzidine (DAB; Sigma Aldrich). Sections were counterstained with cresyl violet (Sigma Aldrich).

For immunohistochemical detection of VCAM-1, 10-μm coronal sections were incubated for 16 h at 4 °C with the primary anti–VCAM-1 antibody (1:250; Millipore). After rinsing with PBS, sections were incubated for 2 h with a biotinylated rabbit anti-rat IgG secondary antibody (1:250; Vector Laboratories). VCAM-1 staining was detected using a standard DAB/hydrogen reaction, and sections were counterstained with cresyl violet.

For immunofluorescent colocalization of tumors and VCAM-1, we used fluorescent tyramide signal amplification (Perkin-Elmer). Sections were quenched with 1% hydrogen peroxide and then streptavidin- and biotin-blocked (15 min each, SP-2002; Vector Laboratories) followed by 30 min incubation in Tris·NaCl blocking buffer (TNB; PerkinElmer). Sections were incubated for 16 h at 4 °C with the primary anti–VCAM-1 antibody (1:200; Millipore) in TNB. After rinsing with PBS, slides were incubated with a rabbit anti-rat IgG secondary antibody (1:250; Vector Laboratories) in TNB for 30 min, washed with PBS, incubated with streptavidin-HRP (1:200; PerkinElmer) in TNB for 30 min, washed, and incubated for 8 min in the dark with tyramide signal amplification–biotin (1:100; PerkinElmer) in dilution buffer. Slides were washed and incubated with a streptavidin-Cy3 fluorophore (1:100; Invitrogen) for 30 min. Slides were cover-slipped using Vectashield mounting medium containing DAPI (Vector Laboratories) to stain nuclei.

Images were acquired using an inverted confocal microscope (LSM-710; Carl Zeiss Microimaging) and analyzed using Image J (rsbweb.nih.gov) and Zen (Carl Zeiss) software. Detection ranges were set to eliminate cross-talk between fluorophores: 409–485 nm for DAPI, 494–553 nm for Alexa Fluor, and 564–712 nm for Cy3.

Analysis of Immunohistochemical and Immunofluorescence Data. To quantify the temporal progression of the number and area of tumors in the 4T1-injected mice, every 10th immunohistochemical section was examined under 20× magnification, and the location of each tumor was marked on a mouse brain atlas template (Allen Brain Atlas; www.brain-map.org) corresponding to that particular brain section. The number of squares contained within each tumor on a square 10 × 10 eye-piece graticule (grid) at 40× magnification were counted and recorded on the atlas template. Every square in the grid corresponded to 625 μm^2, thus allowing calculation of the total tumor area. The total area of every brain section was also measured to calculate the total area of the brain analyzed. Data are given as mean tumor area or number per millimeter squared brain area for either $n = 3$ (day 5) or $n = 4$ (days 10 and 13).

To determine the spatial correlation between tumors and VCAM–MPIO/MRI detection at day 10 after 4T1 injection, the whole brain was assessed in three mice for the volume and location of all metastases. The volume of each metastasis was determined by summing the volumes in every third tissue section and interpolating the volumes of intermediary sections. Tumor location was marked onto a series of mouse brain atlas templates, such that each template equated to five immunohistochemical sections and thus spanned a region of brain ∼150-μm thick. In a similar manner, hypointensities on individual T_2*-weighted images were marked onto a second set of brain atlas templates with a one to one correspondence between images and templates. Subsequently, the two sets of templates were compared for colocalization of tumors detected by immunohistochemistry and MRI. Metastases that were found in the same location as hypointensities were scored as MRI-positive. Those metastases that did not colocalize were scored as MRI-negative.

In the same three 4T1-injected mice (day 10), immunofluorescent microscopy was used to determine the colocalization between VCAM-1 expression on blood vessels and tumor colonies. On every third section throughout the whole brain, metastases were defined as VCAM-1–positive if VCAM-1 staining was observed on a vessel in direct contact with the metastasis; all other metastases were counted as VCAM-1–negative.

Immunohistochemistry: Human Tissue. Twelve cases of human brain metastasis, together with one normal brain sample and one VCAM-1–positive control brain sample (nonspecific inflammation), were examined to assess VCAM-1 up-regulation (ethics reference 06/Q1604/141); 4- to 6-μm-thick sections were cut from paraffin-embedded, formalin-fixed surgical or autopsy material and processed for H&E stains. For immunohistochemistry, sections were dewaxed, rehydrated, and quenched. An anti-human VCAM-1 primary antibody (ATCCHB10519) was used and visualized with the Dako Envision Kit and DAB as the chromogen.

Statistics. For the MRI data, tumor counts, and tumor area measurements, ANOVA was used to identify overall significant differences. Subsequent pair-wise unpaired t tests, with a Welch's correction for unequal variances, were used to identify specific differences between groups. The relationship between tumor number or area (per millimeter squared brain area) and the volumes of VCAM–MPIO hypointensity were tested using a bivariate correlation analysis. All data are expressed as mean ± SEM.

1. Shapiro EM, et al. (2004) MRI detection of single particles for cellular imaging. *Proc Natl Acad Sci USA* 101:10901–10906.
2. Haacke EM, Xu Y, Cheng YC, Reichenbach JR (2004) Susceptibility weighted imaging (SWI). *Magn Reson Med* 52:612–618.
3. Grabner G, et al. (2012) Longitudinal brain imaging of five malignant glioma patients treated with bevacizumab using susceptibility-weighted magnetic resonance imaging at 7 T. *Magn Reson Imaging* 30:139–147.
4. Campbell SJ, et al. (2007) Immunomodulatory effects of etanercept in a model of brain injury act through attenuation of the acute-phase response. *J Neurochem* 103:2245–2255.
5. Wilcockson DC, Campbell SJ, Anthony DC, Perry VH (2002) The systemic and local acute phase response following acute brain injury. *J Cereb Blood Flow Metab* 22:318–326.
6. Blond D, Campbell SJ, Butchart AG, Perry VH, Anthony DC (2002) Differential induction of interleukin-1beta and tumour necrosis factor-alpha may account for specific patterns of leukocyte recruitment in the brain. *Brain Res* 958:89–99.

7. Campbell SJ, et al. (2003) CINC-1 is an acute-phase protein induced by focal brain injury causing leukocyte mobilization and liver injury. *FASEB J* 17:1168–1170.
8. Campbell SJ, et al. (2005) Central nervous system injury triggers hepatic CC and CXC chemokine expression that is associated with leukocyte mobilization and recruitment to both the central nervous system and the liver. *Am J Pathol* 166:1487–1497.
9. Bautista AP, Schuler A, Spolarics Z, Spitzer JJ (1992) In vivo latex phagocytosis primes the Kupffer cells and hepatic neutrophils to generate superoxide anion. *J Leukoc Biol* 51:39–45.
10. Dykstra T, Utermoehlen O, Haas A (2011) Defined particle ligands trigger specific defense mechanisms of macrophages.. *Innate Immun* 17:388–402.

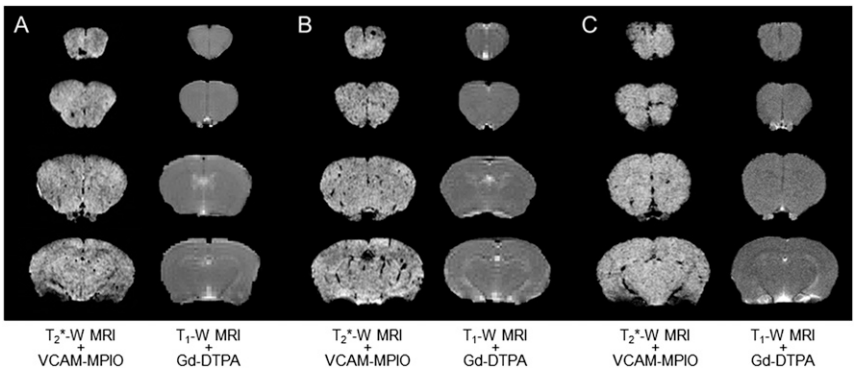

Fig. S1. Absence of BBB breakdown in VCAM–MPIO-enhancing regions. T_2*-weighted and post–gadolinium-DTPA (Gd-DTPA)T_1-weighted images from BALB/c mice either 10 (*A*) or 13 (*B*) d after injection of 4T1 cells or SCID mice 21 d after injection of MDA231BR cells (*C*). After Gd-DTPA injection, T1-weighted images showed no contrast enhancement, indicating a lack of BBB breakdown, despite the appearance of focal areas of signal hypointensity corresponding to endovascular VCAM–MPIO binding.

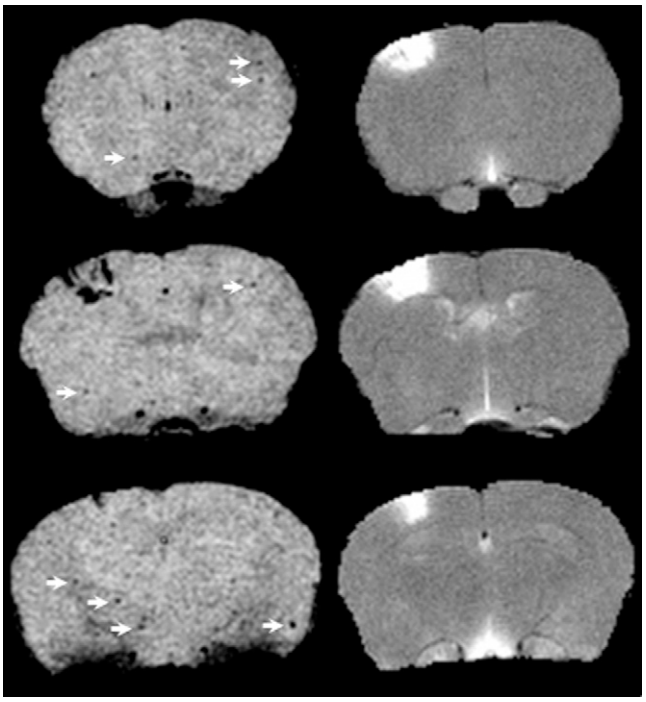

Fig. S2. T2*-weighted images (*Left*) and corresponding post–Gd-DTPA T1-weighted images (*Right*) from the MDA231-BR–injected mouse that showed clinical symptoms at day 20. A single area of Gd-DTPA enhancement was observed in the left motor cortex, which corresponded to an area of intense VCAM–MPIO contrast. However, the contrast patterns are distinct, indicating that the VCAM–MPIO were still endovascularly bound, whereas the Gd-DTPA had clearly extravasated into the parenchyma over a broader region. Interestingly, in this animal, other areas of VCAM–MPIO contrast were evident elsewhere in the brain (arrows), with no concomitant Gd-DTPA enhancement. These findings indicate that, even when clinical symptoms and Gd-detectable metastases become apparent, the VCAM–MPIO approach reveals additional tumor burden that remains undetectable by conventional means.

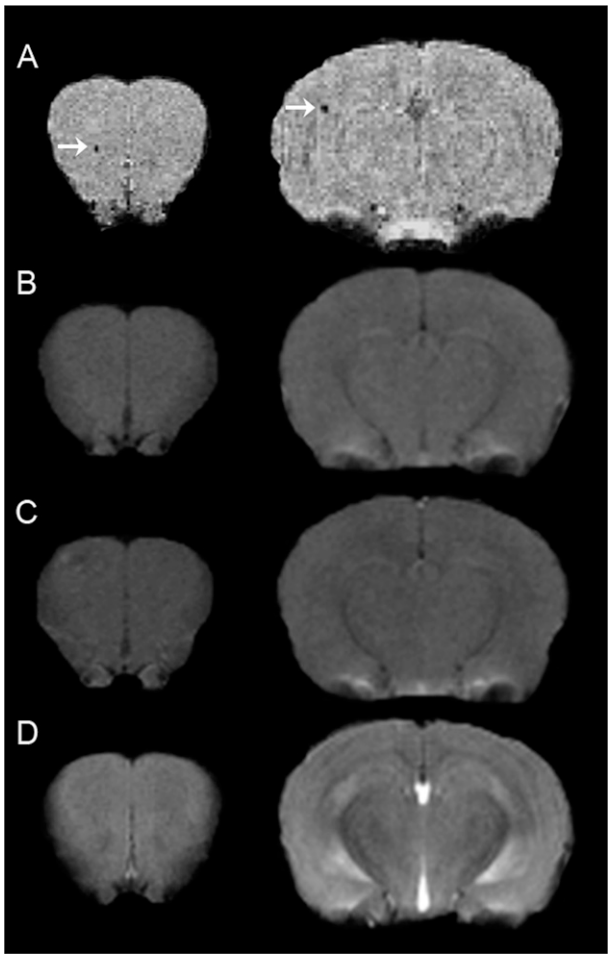

Fig. S3. Selected T2*-weighted images and corresponding pre- and post–Gd-DTPA (clinical dose) T1-weighted images and T2-weighted images acquired post–Gd-DTPA (high dose) at day 10. In the two T2*-weighted images shown (*A*), focal hypointensities are clearly visible, indicating binding of VCAM–MPIO (arrows). The corresponding T1-weighted images acquired pre- (*B*) and post- (*C*) injection of a clinically relevant dose of Gd-DTPA (57.4 mg/kg) showed no signal abnormalities or breakdown of the BBB at the site of VCAM–MPIO binding. No evidence of Gd-DTPA accumulation was found anywhere in the brain with this dose of Gd-DTPA. As for the lower dose, after injection of the higher dose of Gd-DTPA used for the majority of this work (approximately six times the clinical dose), no Gd-DTPA accumulation was found in this animal, and a post–Gd-DTPA T2-weighted dataset (*D*) indicated no evidence of conflicting negative T2 contrast effects that could counteract the positive T1 contrast effect associated with Gd-DTPA accumulation. These findings were consistent across all three animals imaged, and they indicate that the VCAM–MPIO approach reveals tumors that are undetectable by current clinical Gd-DTPA enhancement regimens.

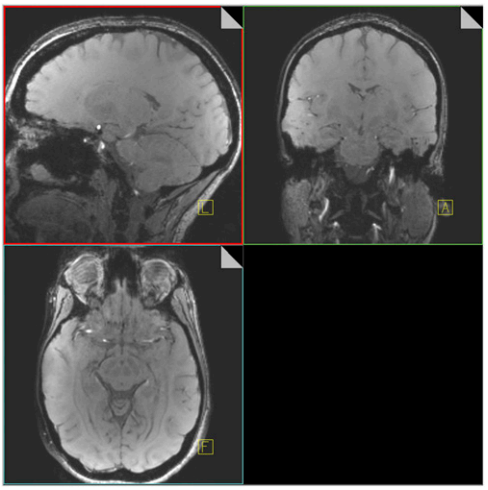

Fig. S4. Representative sagittal, coronal, and axial images from a 3D GE dataset of the human brain. Data were acquired on a 3-T (Siemens) clinical scanner equipped with a 32-channel head coil (Siemens). Acquisition parameters were modified from those parameters used on the 7-T experimental system to match the contrast at 3 T given the known relationships between relaxation times and field strength. A standard 3D GE acquisition was used with 1.0 mm^3 voxels, TE = 17.5 ms (7.5 ms at 7 T), TR = 50 ms (65 ms at 7 T), flip angle = 27°, and bandwidth = 200 Hz/pixel. An acceleration factor of three was used (GRAPPA), and whole-brain coverage was achievable with a single signal average in an acquisition time of 9.5 min. Analysis was performed using a region of interest drawn in the Syngo viewing tool (Siemens), and assessment was made of the mean and SD of regions of interest within white and gray matter.

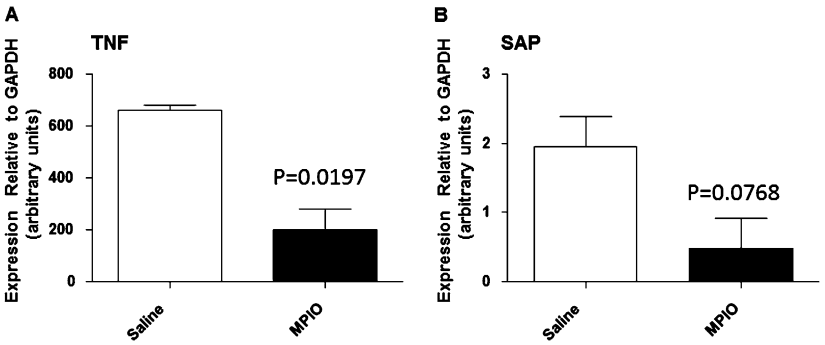

Fig. S5. Graphs showing changes in (*A*) TNF and (*B*) SAP in mouse liver 4 h after i.v. administration of either saline (vehicle) or VCAM–MPIO (4 mg Fe/kg body weight in 100 μL). Data are expressed in arbitrary units relative to GAPDH expression. In both cases, a significant difference was observed between the saline- and VCAM–MPIO-injected animals, indicating induction of an antiinflammatory rather than a proinflammatory phenotype in the liver.